

Processing and characterization of porous Ti_2AlC with controlled porosity and pore size

Liangfa Hu^a, Rogelio Benitez^b, Sandip Basu^b, Ibrahim Karaman^{a,b},
Miladin Radovic^{a,b,*}

^a Materials Science and Engineering Program, Texas A&M University, College Station, TX 77843, USA

^b Department of Mechanical Engineering, Texas A&M University, College Station, TX 77843, USA

Received 30 March 2012; received in revised form 22 June 2012; accepted 20 July 2012

Available online 11 September 2012

Abstract

In this work, we demonstrate a simple and inexpensive way to fabricate porous Ti_2AlC , one of the best studied materials from the MAX phase family, with controlled porosity and pore size. This was achieved by using NaCl as the pore former, which was dissolved after cold pressing but before pressureless sintering at 1400 °C. Porous Ti_2AlC samples with a volume fraction of porosity ranging from ~10 to ~71 vol.% and different pore size ranges, i.e. 42–83, 77–276 and 167–545 μm , were successfully fabricated. Fabricated samples were systematically characterized to determine their phase composition, morphology and porosity. Room temperature elastic moduli, compressive strength and thermal conductivity were determined as a function of porosity and/or pore size. For comparison, several samples pressureless-sintered without NaCl pore former, or fabricated by spark plasma sintering, were also characterized. The effects of porosity and/or pore size on the room temperature elastic moduli, compressive strength and thermal conductivity of porous Ti_2AlC are reported and discussed in this work. It follows that porosity can be a useful microstructural parameter to tune mechanical and thermal properties of Ti_2AlC .

Published by Elsevier Ltd. on behalf of Acta Materialia Inc.

Keywords: MAX phases; Porosity; Elastic moduli; Compressive strength; Thermal conductivity

1. Introduction

Ti_2AlC is one of the most studied compounds out of more than 70 ternary carbides and nitrides with a general formula $\text{M}_{n+1}\text{AX}_n$ (where $n = 1$ to 3, M is an early transition metal, A is an A group element and X is C and/or N) that are commonly referred to as MAX phases [1–3]. These ternary compounds are also sometimes termed metallic ceramics [4] because they possess a useful combination of both metallic and ceramic properties. Ti_2AlC , similar to the rest of the MAX phases, possesses some metal-like properties, i.e. it is readily machinable, thermal-shock-

resistant, thermally and electrically conductive, anomalously soft (Vickers hardness of 4.5 GPa) [3] and damage tolerant [2]. On the other hand, like ceramics, Ti_2AlC has a relatively low coefficient of thermal expansion ($8.2 \times 10^{-6} \text{ }^\circ\text{C}^{-1}$) [3], and it is refractory, elastically stiff (Young's modulus of 277 GPa [5]) and exceptionally oxidation-resistant [6,7]. The combination of both metallic and ceramic properties of Ti_2AlC and other MAX phases originates partially from the metallic nature of the bonding, and partially from their layered structure. This unique combination makes them promising for many applications such as electrical heating elements [8], gas burner nozzles in corrosive environments, high temperature bearings [9], cladding materials in lead-cooled fast-breeder nuclear reactors [10], high temperature electrodes [11], etc.

Most of the studies published to date have reported on processing, structure and properties of the Ti_2AlC and

* Corresponding author at: Materials Science and Engineering Program, Texas A&M University, College Station, TX 77843, USA. Tel.: +1 979 845 5114.

E-mail address: mradovic@tamu.edu (M. Radovic).

Report Documentation Page			Form Approved OMB No. 0704-0188		
Public reporting burden for the collection of information is estimated to average 1 hour per response, including the time for reviewing instructions, searching existing data sources, gathering and maintaining the data needed, and completing and reviewing the collection of information. Send comments regarding this burden estimate or any other aspect of this collection of information, including suggestions for reducing this burden, to Washington Headquarters Services, Directorate for Information Operations and Reports, 1215 Jefferson Davis Highway, Suite 1204, Arlington VA 22202-4302. Respondents should be aware that notwithstanding any other provision of law, no person shall be subject to a penalty for failing to comply with a collection of information if it does not display a currently valid OMB control number.					
1. REPORT DATE 2012		2. REPORT TYPE		3. DATES COVERED 00-00-2012 to 00-00-2012	
4. TITLE AND SUBTITLE Processing and characterization of porous Ti2AlC with controlled porosity and pore size			5a. CONTRACT NUMBER		
			5b. GRANT NUMBER		
			5c. PROGRAM ELEMENT NUMBER		
6. AUTHOR(S)			5d. PROJECT NUMBER		
			5e. TASK NUMBER		
			5f. WORK UNIT NUMBER		
7. PERFORMING ORGANIZATION NAME(S) AND ADDRESS(ES) Texas A&M University, Department of Mechanical Engineering, College Station, TX, 77843			8. PERFORMING ORGANIZATION REPORT NUMBER		
9. SPONSORING/MONITORING AGENCY NAME(S) AND ADDRESS(ES)			10. SPONSOR/MONITOR'S ACRONYM(S)		
			11. SPONSOR/MONITOR'S REPORT NUMBER(S)		
12. DISTRIBUTION/AVAILABILITY STATEMENT Approved for public release; distribution unlimited					
13. SUPPLEMENTARY NOTES					
14. ABSTRACT In this work, we demonstrate a simple and inexpensive way to fabricate porous Ti2AlC, one of the best studied materials from the MAX phase family, with controlled porosity and pore size. This was achieved by using NaCl as the pore former, which was dissolved after cold pressing but before pressureless sintering at 1400 C. Porous Ti2AlC samples with a volume fraction of porosity ranging from 10 to 71 vol.% and different pore size ranges, i.e. 42?83, 77?276 and 167?545 lm, were successfully fabricated. Fabricated samples were systematically characterized to determine their phase composition, morphology and porosity. Room temperature elastic moduli compressive strength and thermal conductivity were determined as a function of porosity and/or pore size. For comparison, several samples pressureless-sintered without NaCl pore former, or fabricated by spark plasma sintering, were also characterized. The effects of porosity and/or pore size on the room temperature elastic moduli, compressive strength and thermal conductivity of porous Ti2AlC are reported and discussed in this work. It follows that porosity can be a useful microstructural parameter to tune mechanical and thermal properties of Ti2AlC.					
15. SUBJECT TERMS					
16. SECURITY CLASSIFICATION OF:			17. LIMITATION OF ABSTRACT Same as Report (SAR)	18. NUMBER OF PAGES 12	19a. NAME OF RESPONSIBLE PERSON
a. REPORT unclassified	b. ABSTRACT unclassified	c. THIS PAGE unclassified			

the rest of the MAX phases in the compact, fully dense state, with the exception of very few recent studies that focused on these materials in the porous state [12–17]. Porous MAX phases deserve systematic studies, because control of the porosity and pore size can be used to tailor their mechanical and functional properties, especially mechanical damping, as was demonstrated by Fraczkiewicz et al. [12] and Sun et al. [14] for Ti_3SiC_2 , and Zhou et al. [13] for Ti_2AlC . Moreover, it has been shown recently that a new class of high-strength MAX phases/Mg composites with exceptional mechanical damping can be easily and inexpensively fabricated by metal (Mg) melt infiltration of porous MAX phases preforms [18–20]. Ti_2AlC /nanocrystalline Mg–matrix composite exhibited higher strength levels in both tension (350 ± 40 MPa) and compression (700 ± 10 MPa) than other Mg composites, as well as exceptional damping capabilities [18]. Apart from structural applications, porous MAX phases have also been demonstrated to be potentially good candidate materials for substrates for catalytic coatings in gas exhaust catalyst devices [21].

In this limited number of studies, porous MAX phases were prepared by using one of two methods: (1) incomplete densification during sintering of MAX phase powders or reaction sintering of elemental powders [12–17], or (2) the replica template method from the highly dispersed aqueous suspension using polyurethane sponges as a template [21]. Although the first method is simple and straightforward, it does not allow good control over morphology, volume fraction and size of the pores. On the other hand, the second method allows good control of the pore size and morphology, but it is quite complex and time consuming, and cannot be used for processing samples with a low volume fraction of porosity.

In this work, a simple and inexpensive way of fabricating porous Ti_2AlC with a controlled volume fraction of porosity and pore size using NaCl as the pore former is reported. The use of NaCl as the pore former was first reported by Polonsky and co-workers [22] in the 1960s to fabricate aluminum foams. Since then, this method has been utilized to fabricate open-cell aluminum foams [23–25], shape memory alloy foams [26,27], titanium foams [28] and other porous metals [29,30]. This inspired us to process porous Ti_2AlC using NaCl powders as the pore former. NaCl can be easily and completely removed by dissolving in water after cold pressing but before sintering. Therefore, no reaction between the pore former and the MAX phase is expected, unlike in the case of organic pore formers that can react with the MAX phase powders during sintering and form binary carbides if they are not burned out completely at lower temperatures [31]. Additionally, NaCl is cheap and commercially available in a broad range of particle sizes, which allows an inexpensive way to control pore size. The microstructure of porous Ti_2AlC was systematically characterized, as well as room temperature elastic moduli, compressive strength and thermal conductivity to elucidate the effect of porosity and pore

size on the thermal and mechanical properties of Ti_2AlC . The latter was based on the comparison of different samples pressureless-sintered both with and without using NaCl pore former, as well as several samples sintered using spark plasma sintering (SPS). Furthermore, we demonstrate that the developed methodology can be implemented easily to process the samples with graded porosity, and consequently functionally graded properties of the MAX phases.

2. Experimental procedures

Ti_2AlC powders (Kanthal AB, Sweden) with a particle size of 45–90 μm or <20 μm were used to process all samples in this study. Fig. 1a shows a field emission scanning electron microscopy (FE-SEM) image of Ti_2AlC powder with a particle size of 45–90 μm , while the inset in the top-right corner illustrates the nanolaminated nature of the Ti_2AlC powders. NaCl powders with particle sizes of 45–90 μm , 180–250 μm and 355–500 μm were used as the pore former (Fig. 1b). The Ti_2AlC and NaCl powder mixtures with 0, 20, 40, 60 and 80 vol.% NaCl pore former were mixed for 1 h by ball milling and cold pressed in the cylindrical steel die (12.7 mm in diameter) using a pressure of 800 MPa. Green bodies were soaked in water overnight to dissolve the NaCl pore former, and rinsed in water after that several times to remove all remaining NaCl. The green bodies were then pressureless-sintered in flowing argon at 1400 °C for 4 h. A Ti_2AlC sample with graded porosity was also prepared using this method, but the steel die was filled in this case with four different layers containing 0, 20, 40 and 60 vol.% NaCl pore former. For comparison, some porous samples were prepared by incomplete densification using spark plasma sintering (SPS25–10, Thermal Technologies, CA) of Ti_2AlC powders in the 1100–1200 °C temperature range under 50–100 MPa for 20 min.

The microstructure of the processed samples was characterized using a field emission scanning electron microscope (FE-SEM; Quanta 600 FEG, FEI, Oregon, USA or JSM-7500F, JEOL, Tokyo, Japan). Pore size distribution was determined by measuring the size of over 30 pores using the intercept method, ASTM E112–10, from the SEM images in the four randomly selected locations on each sample, and calculating the fraction of the pores with the size in the certain range. The density, overall porosity and open porosity of the sintered samples were determined by the alcohol immersion method based on Archimedes' principle, as specified in ASTM C20-00 using the following equations:

$$\rho = \frac{m_{\text{dry}} \times \rho_{\text{ethanol}}}{m_{\text{wet}} - m_{\text{suspended}} + m_{\text{wire}}} \quad (1)$$

$$P_{\text{overall}} = \left(1 - \frac{\rho}{\rho_{\text{theoretical}}} \right) \times 100 \quad (2)$$

$$P_{\text{open}} = \frac{m_{\text{wet}} - m_{\text{dry}}}{m_{\text{wet}} - m_{\text{suspended}} + m_{\text{wire}}} \times 100 \quad (3)$$

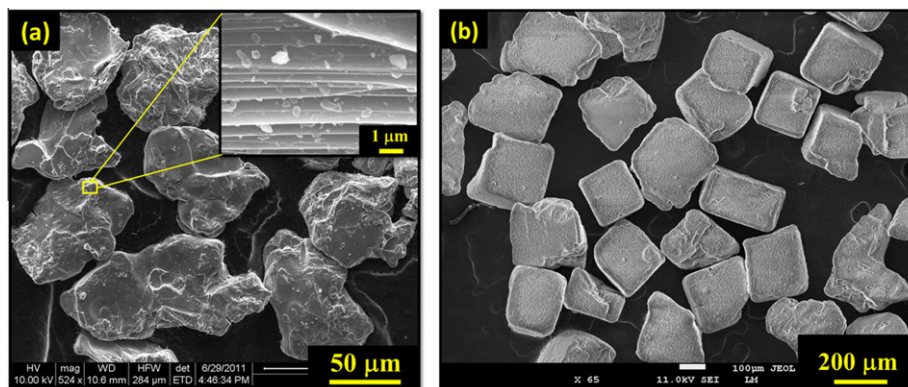


Fig. 1. FE-SEM images of (a) Ti_2AlC powder with particle size of 45–90 μm , and (b) NaCl powder with particle size of 180–250 μm . The inset illustrates the nanolaminated structure of Ti_2AlC .

where m_{dry} is the dry mass (in g) of the sample, $m_{\text{suspended}}$ is the mass of the sample suspended in 200% proof ethanol, m_{wet} is the mass of the sample after soaking in the ethanol, m_{wire} is the mass of the suspending system, ρ_{ethanol} is the density (g cm^{-3}) of the ethanol, P_{overall} is volume fraction of the overall porosity (vol.%) of the sample and P_{open} is volume fraction of the open porosity of the sample. The theoretical density of 4.11 g cm^{-3} [1] for fully dense Ti_2AlC was used as a reference to calculate the volume fraction of overall porosity, Eq. (2). The phase composition of starting Ti_2AlC powder and sintered Ti_2AlC sample was determined using an X-ray diffractometer (XRD; D8 Discover, Bruker, Madison, USA) with $\text{Cu } K_{\alpha}$ radiation (wavelength = 1.542 Å) at 40 kV and 30 mA. The 2θ range was varied from 8° to 80° with a step size of 0.04° and a step time of 1.5 s. The scanning results were analyzed utilizing the Inorganic Crystal Structure Database (ICSD).

Elastic moduli of the processed samples were measured by resonant ultrasound spectroscopy (RUS; Magnaflux Quasar Systems, NM), which is based on measuring the spectrum of the resonant mechanical vibrations for a specimen with known geometry, dimensions and mass [5,32,33]. All samples for RUS were machined until sharp edges and a parallelism with less than 1% error of thickness were achieved. Porous Ti_2AlC specimens (12.7 mm or 25.4 mm in diameter and 3.5 mm in thickness) were placed on three piezoelectric transducers. One of the transducers (the transmitting transducer) generates an elastic wave at constant amplitude but varying frequency, whereas the other two transducers detect a response from the sample, i.e. resonant spectrum. The Young's, bulk and shear modulus, as well as Poisson's ratio, were determined from the measured resonant spectrum, using the multidimensional algorithm Quasar RuSpec (Magnaflux Quasar Systems, NM) that iteratively minimizes error between the measured and calculated resonant peaks by changing the initially "guessed" elastic constants, until converging values are achieved. The compressive strength of the samples with dimensions of $5 \times 5 \times 8$ mm was measured by using a universal testing machine (MTS810, MTS, MN) under displacement control

mode with a strain rate of $5 \times 10^{-3} \text{ s}^{-1}$. Teflon tape was applied between sample and fixture to reduce the effects of friction. All samples for compressive testing were cut with a diamond saw and additionally ground to achieve parallelism with less than 1% error of thickness.

Room temperature thermal conductivity of the porous Ti_2AlC was measured using a hot disk thermal constants analyzer (TPS 2500, Hot Disk AB, Gothenburg, Sweden). The hot disk sensor with radius of 2.001 mm consists of an electrically conducting pattern in the shape of a double spiral which is laminated between two thin sheets of insulating material (Kapton). The sensor was sandwiched between two pieces of 25.4 mm diameter discs of Ti_2AlC (thickness 7–10 mm) during measurement. Because these samples were bigger than the samples for microstructure characterization, a lower cold press load (400 MPa) was used due to the load limit of the cold press.

3. Results and discussions

3.1. Phase identification

Fig. 2 shows a selected, but typical, XRD spectrum of a porous Ti_2AlC sample which was prepared with 40 vol.% of NaCl pore former with a particle size of 355–500 μm , as well as an XRD spectrum of the starting Ti_2AlC powder. No new phase was observed in the porous Ti_2AlC sample after sintering. Two major phases in both starting powders and pressureless sintered samples (Table 1 and Fig. 2) are Ti_2AlC and Ti_3AlC_2 , while Al_2O_3 and TiC were present only in a small amounts as impurities. The molar fractions of different phases in Table 1 were determined by normalizing the intensity of the highest XRD peaks for each phase. More importantly, no presence of NaCl was observed in the sintered porous sample, which indicates that all NaCl pore former was completely removed during the dissolving in water. This was also confirmed by energy-dispersive spectroscopy (EDS; results not shown here).

When comparing the phase composition of the starting powder and sintered sample it can be noticed that the

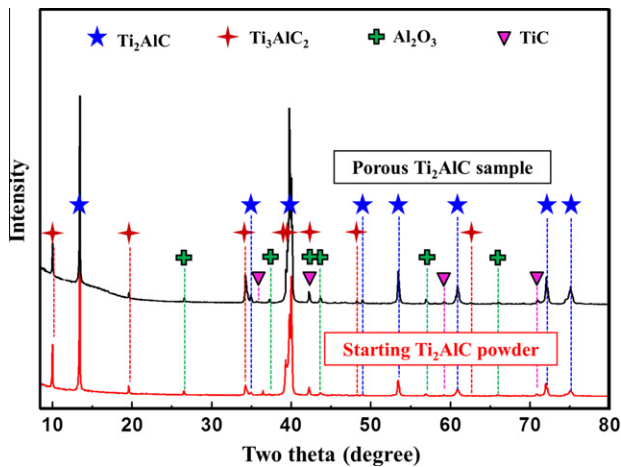
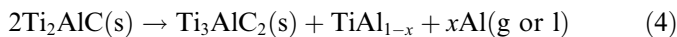


Fig. 2. XRDs of starting Ti_2AlC powder and porous Ti_2AlC sample prepared with 40 vol.% of NaCl pore former with 355–500 μm particle size. The identification of phases was according to the Inorganic Crystal Structure Database (ICSD) collection code 165460 for Ti_2AlC , 153266 for Ti_3AlC_2 , 10425 for Al_2O_3 and 44494 for TiC , respectively.

amount of Ti_2AlC and TiC decreases, while the amount of Ti_3AlC_2 increases, during pressureless sintering at 1400 °C. The latter can be explained by the reaction of Ti_2AlC with TiC to form Ti_3AlC_2 . However, a decrease of the amount of TiC during sintering is negligible when compared to the decrease of the amount of Ti_2AlC or increase of the amount of Ti_3AlC_2 . Thus, the change in the phase composition must be predominately caused by decomposition of Ti_2AlC to Ti_3AlC_2 according to the following reaction [34]:



where $x \leq 1$. The composition of TiAl_{1-x} in Reaction (4) depends on how much Al is lost to the surroundings [34], with the extreme situation when Al is totally lost as a gaseous or liquid phase and only pure Ti remains. It is this reaction that additionally explains the fact that the decrease of Ti_2AlC is almost two times the increase of Ti_3AlC_2 and that the intensity ratio of $\text{Ti}_2\text{AlC}/\text{Ti}_3\text{AlC}_2$ decreased 10% from 4.0 to 3.6 (Table 3). In the porous sample, decomposition according to Reaction (4) must be even more severe when compared to the fully dense samples, because the high surface area allows faster loss of the Al. Furthermore, a total weight loss of $\sim 1\%$ was observed after sintering, which may be attributed to the loss of Al, even possibly some Ti, that can both vaporize at high temperatures and go to the surroundings. It also follows that the increase of Al_2O_3 is not surprising because some of the Al released from this reaction can react with the residual oxygen in the sintering atmosphere and form Al_2O_3 . Both

lost Al and lost Ti may react with oxygen to form oxides. However, the Gibbs free energy of the $4\text{Al} + 3\text{O}_2 \rightarrow 2\text{Al}_2\text{O}_3$ reaction is more negative than that of the $\text{Ti} + \text{O}_2 \rightarrow \text{TiO}_2$ reaction, [35,36], which indicates that Al reacts with oxygen more easily than Ti. This most likely explains why no TiO_2 peaks (but Al_2O_3 peaks) were detected by XRD in the porous Ti_2AlC sample.

3.2. Characterization of porosity

The porosity was quantitatively characterized by the determining values of overall and open porosities of porous Ti_2AlC samples, as described earlier. Fig. 3 shows the variation of overall and open porosities with volume fraction of NaCl pore former for different sizes of the pore former particles (i.e. 45–90 μm , 180–250 μm , and 355–500 μm) that were used to process porous Ti_2AlC samples with 45–90 μm Ti_2AlC powders. In all cases, the lowest overall porosity of $\sim 9\text{--}10\text{ vol.}\%$, with $\sim 60\%$ open/overall porosity ratio, was measured in the sample pressureless sintered without any NaCl pore former. This porosity is mostly due to the presence of intergranular pores (closed pores) and channels (open pores) that remained in the structure as a result of incomplete densification during the pressureless sintering.

Both overall and open porosities generally increase linearly with increasing volume fraction of NaCl pore former (Fig. 3), and that trend is independent of the particle size of the NaCl pore former. The former is particularly obvious in Fig. 3d, where overall porosity of the samples with different amounts of pore former was plotted vs. volume fraction of pore former. This finding cannot be overemphasized, since it suggests that the size of pore former in general does not affect shrinkage of Ti_2AlC during densification/sintering of the porous samples. However, the overall porosity in sintered Ti_2AlC is not always lower than the volume fraction of pore former added before sintering. Fig. 3 clearly shows that the overall porosity of sintered samples is larger than the volume fraction of pore former for samples processed with less than 40 vol.% of pore former. However, for samples processed with more than 40 vol.% of pore former, the overall porosity is lower than the volume fraction of pore former used in their processing. This observation suggests that porosity in sintered samples is not only a function of the amount of pore former used during processing, but also partially the result of incomplete sintering of Ti_2AlC powder.

Furthermore, Fig. 3 shows that the difference between overall and open porosities generally becomes smaller as

Table 1

Molar fractions of the phases in the starting Ti_2AlC powder and porous Ti_2AlC sample as determined by the relative intensity of the highest XRD peaks of each phase.

Material	Molar fraction of phases, %				Phase ratio $\text{Ti}_2\text{AlC}/\text{Ti}_3\text{AlC}_2$
	Ti_2AlC	Ti_3AlC_2	Al_2O_3	TiC	
Starting Ti_2AlC powder	77.0	19.2	1.3	2.5	4.0
Porous Ti_2AlC sample	74.5	20.7	2.5	2.3	3.6

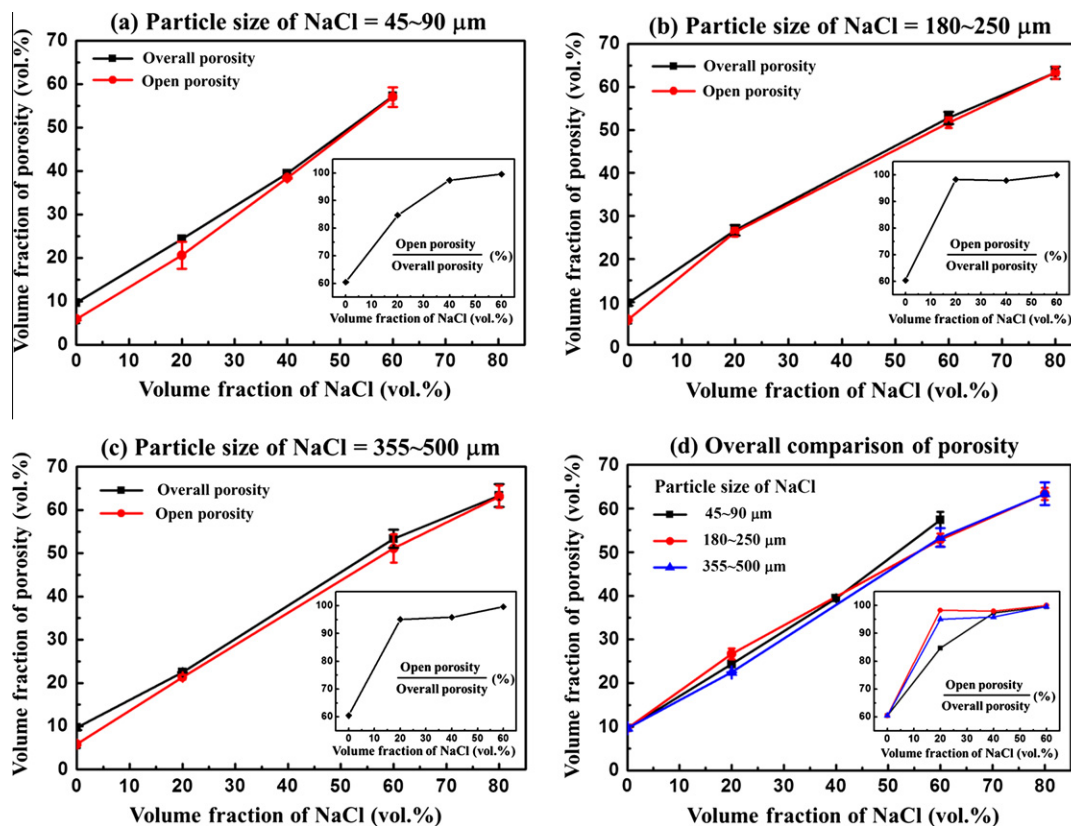


Fig. 3. Variations of overall and open porosities with volume fraction of NaCl pore former. Particle size of NaCl pore former: (a) 45–90 μm , (b) 180–250 μm , (c) 355–500 μm and (d) comparison of overall porosity in all samples. Insets show the open/overall porosity ratio as a function of volume fraction of NaCl pore former.

the volume fraction of NaCl increases. For example, Fig. 3c shows that the open/overall porosity ratio increased from 0.61, 0.95, 0.96 to 0.99 as the volume fraction of NaCl pore former increased from 0, 20, 40 to 60 vol.% (for the samples processed using NaCl pore former with particle size of 355–500 μm). It indicates that the number of the connected pores increases with increasing volume fraction of NaCl pore former. More individual NaCl particles made it easier for any two individual particles to connect to each other, leading to more connectivity among pores and making them open. Fig. 3 also suggests that when the size of the pore former is significantly larger than the powder size (inserts in Fig. 3b and c), almost all pores are interconnected when the porosity is above only 20%. However, when the pore former size is comparable to that of the starting powders, volume fraction of the open porosity increases more gradually with the amount of pore former.

The results discussed above suggest that even higher porosities, especially open porosity, could be achieved using this method if the Ti_2AlC powder is finer. Fig. 4 demonstrates that when starting with the same volume fraction of NaCl pore former, i.e. 80 vol.%, the sample with finer Ti_2AlC powder (<20 μm particle size) reached 71 vol.% overall porosity, which was the highest porosity achieved via this processing method and was 13% higher than the corresponding value of for the sample processed with coarse Ti_2AlC powder (45–90 μm particle size). This result

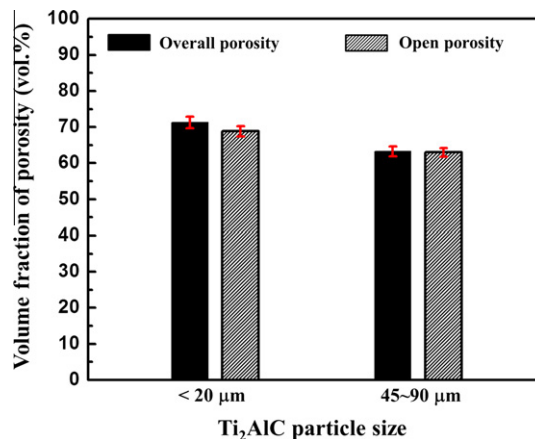


Fig. 4. Variation of overall porosity with the starting Ti_2AlC particle size: fine powder (<20 μm) and coarse powder (45–90 μm). Both samples were processed using 80 vol.% NaCl pore former (180–250 μm).

suggests that the Ti_2AlC powder size, in addition to volume fraction and size of NaCl pore former, is another parameter that can be used to tailor porosity and pore connectivity in porous Ti_2AlC prepared with NaCl pore former.

3.3. Morphology of porous samples and pore size distribution

Fig. 5 shows morphology of the porous Ti_2AlC samples with different pore sizes but the same volume fraction of

NaCl pore former (60 vol.%). All three samples in Fig. 5a–c had relatively comparable porosities of 56.0, 50.9 and 50.6 vol.%, although they were prepared with pore former sizes of 45–90 μm , 180–250 μm and 355–500 μm , respectively. Although pores in Fig. 5a appear to be more connected than that in both Fig. 5b and c, results shown in Fig. 3 clearly demonstrate that that is not the case because all three samples have comparable volume fractions of open porosity. The fracture surface of the porous Ti_2AlC sample in Fig. 5d illustrates even better the typical connectivity of Ti_2AlC grains and formation of the sintering necks between them. The strong network of grains with a well-developed necks is critical to obtain high mechanical strength of porous samples (see below). Note that the laminated nature of Ti_2AlC could be once again clearly observed at the walls of the pores, as illustrated in the inset in Fig. 5d.

Fig. 5 also shows that the pore shape became more and more elliptical with increasing pore size. The elliptical pores have conjugate in the loading direction, i.e. vertical direction in Fig. 5, and transverse diameter perpendicular to loading direction during cold pressing. Taking into account that the shape of NaCl pore former particles is cubic-like (Fig. 1b) rather than elliptical, the elliptical

shape of the pores is most likely a consequence of the cold pressing because larger NaCl pore former particles deform, and eventually crush and compact easier, in the direction of cold-press loading. The optical microscopy on the cross-sectional surface of as-pressed samples (not show here) confirmed the latter.

The pore size distributions were quantitatively characterized by measuring the pore sizes in the samples shown in Fig. 5, and the results are summarized in Table 2 and Fig. 6. Table 2 summarizes the average pore sizes and standard deviations for each pore size distribution curve shown in Fig. 6. As expected, the average pore size increases from 59 μm , 148 μm to 346 μm with increasing particle size of NaCl pore former (45–90 μm , 180–250 μm and 355–500 μm). Furthermore, Fig. 6 indicates that the pore size distribution becomes broader with increasing particle size of NaCl pore former. The authors believe that the increasingly broader particle size range of NaCl pore former is the main reason why the pore size range increased significantly. Another reason is that the samples processed from coarser particles have elliptical pore shape, and both transverse and conjugate diameters were taken into account for pore size measurements, which broadened significantly the pore size range. This also

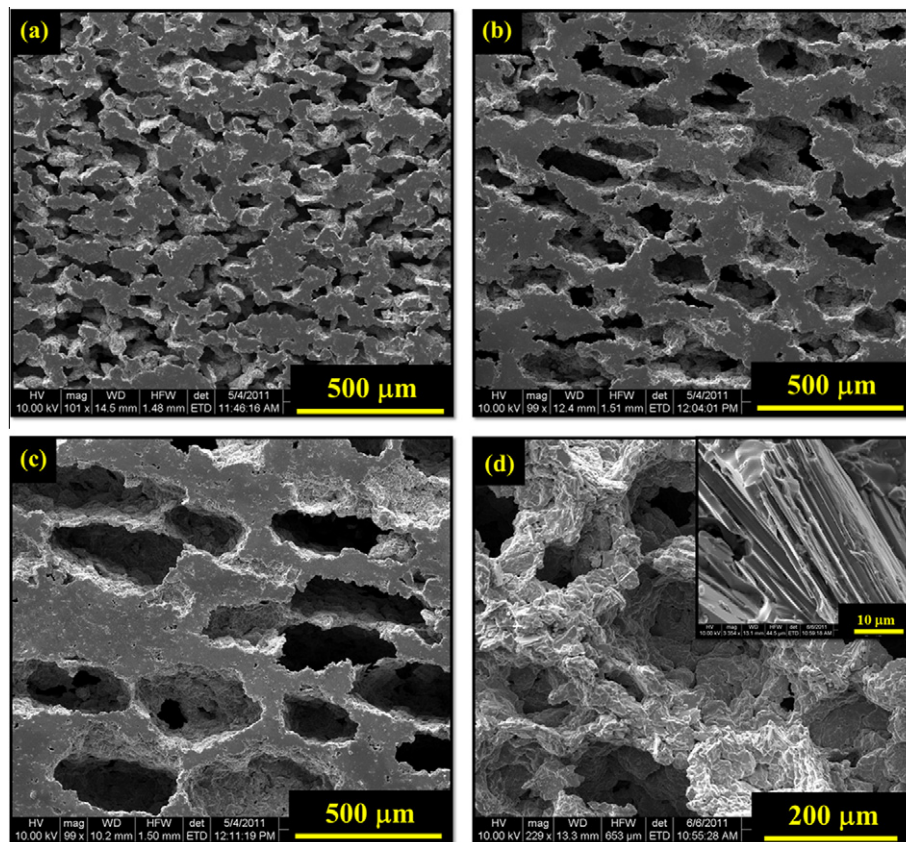


Fig. 5. Morphology of porous Ti_2AlC samples after sintering with different pore sizes formed by the addition of 60 vol.% NaCl pore former with different particle sizes: (a) 45–90 μm , (b) 180–250 μm , (c) 355–500 μm and (d) typical microstructure of fracture surface at higher magnification (60 vol.% NaCl pore former with particle size 180–250 μm). The overall porosity of these samples were comparable: (a) 56.0 vol.%, (b) 50.9 vol.%, (c) 50.6 vol.% and (d) 50.9 vol.%.

Table 2

Pore sizes of porous Ti_2AlC samples with comparable overall porosities. Average pore size and standard deviation were determined from the measured pore size values as $\bar{x} = \frac{1}{N} \sum_{i=1}^N x_i$ and $s = \sqrt{\frac{1}{N} \sum_{i=1}^N (x_i - \bar{x})^2}$ respectively, where N is the total number of the pore size values measured from SEM images, x_i is the pore size value and \bar{x} is the average pore size value.

Particle size of NaCl (μm)	Volume fraction of NaCl (%)	Porosity (vol.%)	Average pore size (μm)	Standard deviation (μm)
45–90	60	56.0	59	11.7
180–250		50.9	148	55.5
355–500		50.6	346	133.1

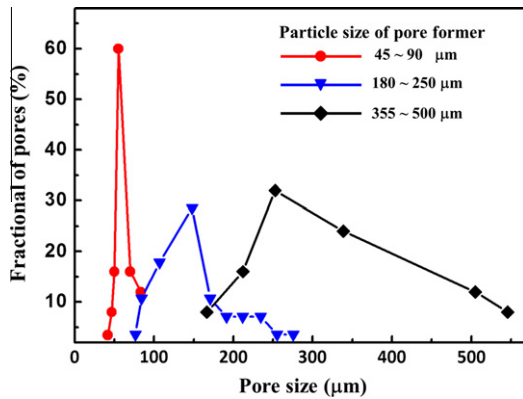


Fig. 6. Pore size distribution of porous Ti_2AlC with different pore sizes formed by NaCl particles with different particle sizes: 45–90 μm , 180–250 μm and 355–500 μm .

explained that the sample processed from 355–500 μm NaCl pore former would have some measured pore size at 550 μm , which is larger than the maximum size of the pore former particles.

Fig. 7 illustrates the morphology of porous Ti_2AlC samples processed with different volume fractions (0, 20, 40 and 60 vol.%) but fixed particle size of 45–90 μm of NaCl pore former. In this case, after dissolving and sintering, porous Ti_2AlC samples without processing cracks were obtained with a maximum porosity of 56.0 vol.%. As illustrated in Fig. 7d, the sample with highest porosity shows interconnected pores which are homogeneously dispersed in the Ti_2AlC matrix. A sample with lower porosity was processed using no NaCl pore former for comparison (Fig. 7a), i.e. only pressureless sintering of starting Ti_2AlC powders.

3.4. Porous sample with graded porosity

The simple and inexpensive fabrication method described above was also applied to fabricate a porous sample with graded porosities as shown in Fig. 8. This sample was made by cold pressing and sintering together four different layers with different volume fraction of NaCl pore former (i.e. 0 vol.%, 20 vol.%, 40 vol.% and 60 vol.%) in one sample. The importance of having a simple and easy method for processing Ti_2AlC samples with graded porosity cannot be overestimated, since it would allow us to functionally grade properties of the MAX phases and their composites.

3.5. Mechanical properties

The elastic moduli of fully dense and porous Ti_2AlC samples, as determined by RUS, are listed in Table 3. The highest porosity of all tested samples is ~ 35 vol.%. The main reason for not testing even higher porosity samples is that high porosity samples were not only too fragile, but also hard to machine to the shape needed for reliable testing under RUS, as well in compression. The Young's and shear moduli were also plotted as functions of porosity in Fig. 9. All relative Young's and shear moduli values are compared with Young's and shear moduli of the fully dense material [37]. Both Young's and shear moduli vs. porosity data were fitted using the exponential model, Hasselman model and composite spheres model (CSM) using the following equations:

Exponential model [38,39]:

$$\frac{E}{E_0} = \frac{G}{G_0} = e^{-b \cdot P} \quad (5)$$

Hasselman model [40]:

$$\frac{E}{E_0} = \frac{G}{G_0} = 1 - \frac{b \cdot P}{1 + (b - 1) \cdot P} \quad (6)$$

Composite spheres model [41–43]:

$$\frac{E}{E_0} = \frac{G}{G_0} = \frac{(1 - P)^2}{1 + b \cdot P} \quad (7)$$

where E_0 and G_0 are the Young's and shear moduli of fully dense Ti_2AlC , P is the porosity and b is an empirical constant. The results of the regression analysis of the experimental data in Fig. 9 using all three models, as well the coefficient of correlation, R^2 , are listed in Table 4. Note that the R^2 values for all three models are essentially the same, suggesting that all three models can be used equally well to describe the change of the elastic moduli of Ti_2AlC with porosity. Nevertheless, most importantly the results shown here suggest that the increasing porosity within the range of 3–35 vol.% causes a sharp decrease in elastic moduli, independent of the different morphology of the pores in the samples that were prepared by different methods, i.e. HIPing [5], SPSing and pressureless sintering. Although the pore morphology is different from SPS samples to pressureless sintered samples, even from pressureless sintered sample with NaCl pore former to those without NaCl pore former, the experimental data for different samples did not scatter significantly, but agreed well

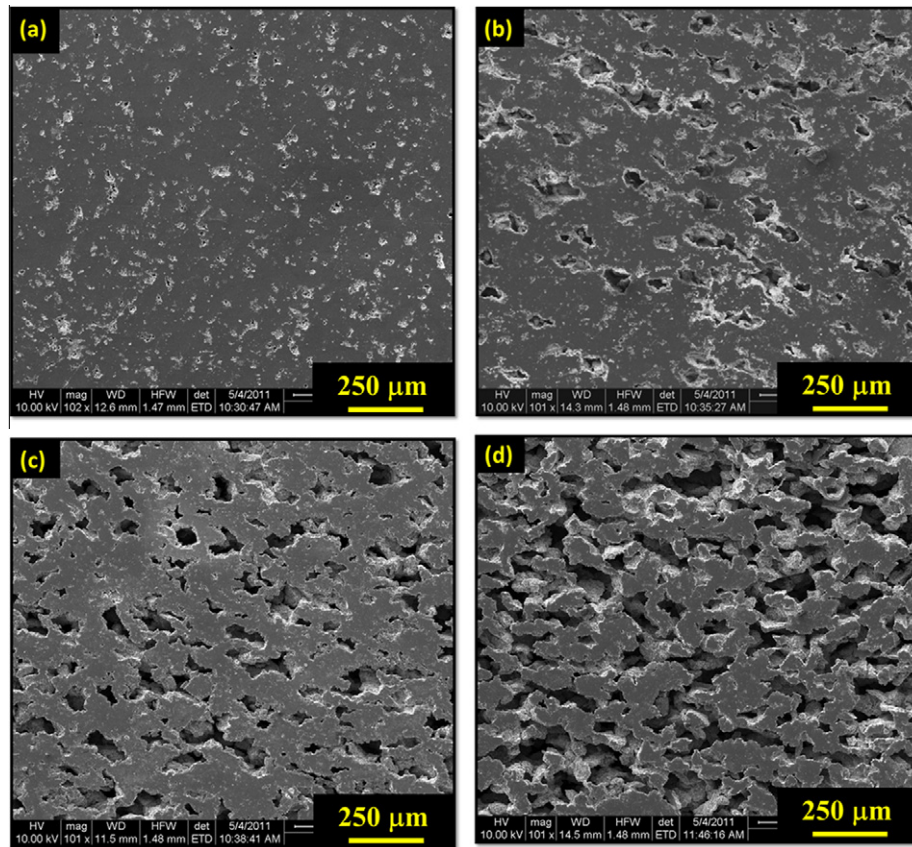


Fig. 7. Morphology of porous Ti_2AlC samples with increasing overall porosity: (a) 9.3 vol.%, (b) 23.6 vol.%, (c) 39.3 vol.% and (d) 56.0 vol.%. Samples (b), (c) and (d) were processed from NaCl pore former with the same particle size (45–90 μm).

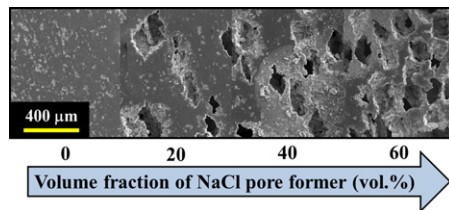


Fig. 8. Micrograph of the porous Ti_2AlC sample with graded porosity. Particle size of the pore former was 180–250 μm . Overall porosity of this sample is 33.2 vol.%.

with the models. Therefore, the decrease of elastic moduli predominately stems from the increasing porosity, regardless of the processing method and pore morphology.

Results of compressive strength measurements are shown in Fig. 10a and summarized in Table 5. The compressive strength of fully dense Ti_2AlC prepared by HIPing [44] was used for comparison and its “relative compressive strength” in Fig. 10a is equal to 1. All tested samples, independent of the volume fraction of porosity, failed by cracking in the direction of approximately 45° relative to the loading direction, as illustrated in Fig. 10b. This observation suggests that even 33 vol.% porous Ti_2AlC shows a somewhat graceful failure, and does not crush and fragment under compression like typical highly porous ceramics. The relative compressive strength of Ti_2AlC decreases down to 0.3 as the porosity increases to 42 vol.%. However,

unlike common ceramics, i.e. Al_2O_3 , yttria stabilized zirconia (YSZ) and Si_3N_4 [45–47], whose compressive strength drops dramatically with increasing porosity, the compressive strength of Ti_2AlC decreases less rapidly and almost linearly with increasing porosity (Fig. 10). The reason for this observation must lie in the kinking and kink band formation that are typical deformation mechanisms in Ti_2AlC , and to a further extent to all MAX phases [1–3]. The SEM images of the fracture surfaces shown in Fig. 11a–c reveal intensive kinking and delamination of porous Ti_2AlC that dissipated a large amount of mechanical energy during crack propagation. Additional evidence of the exceptional damage tolerance of Ti_2AlC could be found in the fact that standard deviations (from 3.9 to 16.0%) for compressive strengths are relatively low, for all tested samples independent of the volume fraction of porosity and pore sizes.

The compressive strength was also investigated as a function of pore size and loading direction (Fig. 11d–f). Three samples with comparable volume fraction porosity, i.e. 29%, 33% and 33%, but processed using NaCl pore former with different particle sizes (i.e. 45–90 μm , 180–250 μm and 355–500 μm , that consequently result in the different average pore sizes (i.e. 55, 148 and 346 μm , respectively), were tested and the results are shown in Fig. 11d. Fig. 11d clearly shows that the compressive strength decreases due to increasing pore sizes. However, this

Table 3
Particle size of starting Ti₂AlC powder, pore former size and volume fraction, sintering method, dimensions of testing samples, density ρ , volume fraction of overall porosity P , shear modulus G , Young's modulus E , Poisson's ratio ν and bulk modulus B of all tested samples.

Sample	Ti ₂ AlC particle size	Pore former size/volume fraction	Processing method	Dimensions (mm)	ρ (g/cm ³)	P (vol.%)	G (GPa)	E (GPa)	ν	B (GPa)	Reference
A	~25 μ m of grain size	None	HIP	Φ 20.20 \times 3.00	4.00	2.7	118.8	277.6	0.169	139.6	[18]
B	45–90 μ m	None	SPS	Φ 19.68 \times 5.17	3.76	8.5	95.2	221.9	0.165	110.5	This work
C	45–90 μ m	None	SPS	Φ 19.68 \times 7.10	3.55	13.6	67.9	158.5	0.167	79.3	
D	45–90 μ m	None	SPS	Φ 19.67 \times 5.94	3.45	16.0	66.0	153.1	0.160	75.1	
E	45–90 μ m	None	SPS	Φ 19.63 \times 7.51	3.41	17.0	57.6	134.2	0.165	66.8	
F	<20 μ m and 45–90 μ m	None	Pressureless sintering	Φ 23.99 \times 3.45	3.54	13.8	88.3	206.9	0.172	105.2	
G	45–90 μ m	None	Pressureless sintering	Φ 12.55 \times 1.81	2.98	27.5	49.1	116.3	0.184	61.4	
H	45–90 μ m	180–250 μ m, 20 vol.%	Pressureless sintering	15.79 \times 15.79 \times 7.55	2.69	34.6	40.9	93.8	0.148	44.4	

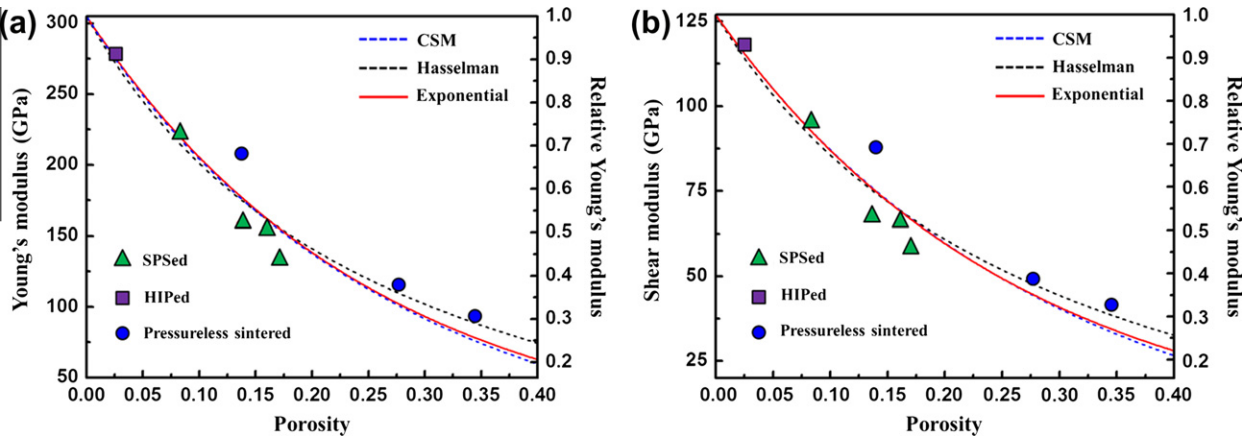


Fig. 9. Young's (a) and shear (b) moduli of Ti₂AlC samples as functions of overall porosity. Data points are experimental data determined from the SPS samples (triangle, green dots), HIP sample (square, purple dot) [5] and pressureless sintered samples (round, blue dots), listed in Table 3. Also included are the predictions from the CSM model (dashed blue line), Hasselman model (dashed black line) and exponential model (solid red line). (For interpretation of the references to colour in this figure legend, the reader is referred to the web version of this article.)

Table 4
Empirical constant b and coefficient of correlation R^2 from the regression analysis of the experiment data and the model values.

Model name	Young's modulus		Shear modulus	
	b	R^2	b	R^2
CSM	2.10	0.92	1.80	0.92
Hasselman	4.65	0.92	4.35	0.92
Exponential	3.95	0.92	3.78	0.92

decrease is relatively moderate, ~38% for the increase in average pore size of over six times, which is also a less rapid drop what the Griffith criterion [48] predicts, i.e. for the strength of brittle materials containing pores:

$$\sigma = (E\gamma/\pi c)^{0.5} \quad (8)$$

where E is the Young's modulus, γ is the surface energy and c is pore size. This observation is yet another indirect evidence illustrating the high damage tolerance of porous Ti₂AlC. To investigate the effect of pore axis orientation with respect to loading direction, specimens from a sample processed with 20 vol.% NaCl pore former (355–500 μ m) were machined

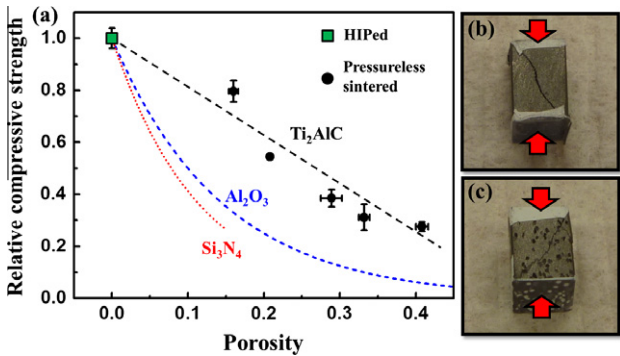


Fig. 10. (a) Relative compressive strength of Ti₂AlC as a function of overall porosity. The loading direction is normal to aligned pore axis. Data points are from experiments on an HIP sample (square, green dot) [35] and pressureless sintered samples (round, black dots), listed in Table 4. Also included are the corresponding data for Al₂O₃ (dashed blue line) [36] and Si₃N₄ (dashed red line) [38]. Compression samples after testing: (b) a Ti₂AlC sample processed without using NaCl pore former, volume fraction of overall porosity = 21%; (c) a Ti₂AlC sample processed using 20 vol.% NaCl pore former (355–500 μ m), volume fraction of overall porosity = 33%. Teflon tape was applied between sample and fixture to reduce the effects of friction. (For interpretation of the references to colour in this figure legend, the reader is referred to the web version of this article.)

Table 5

Particle size of starting Ti_2AlC powder, pore former size and volume fraction, sintering method, dimensions of testing samples, volume fraction of overall porosity P and compressive strength σ of all samples tested for compressive strength.

Sample	Ti_2AlC particle size	Pore former size/volume fraction	Processing method	Dimensions (mm)	P (vol.%)	σ (MPa)	Reference
SA	20–25 μm of grain size	None	HIP	$2 \times 2 \times 2$	Fully dense	540 ± 21	[19]
SB	$<20 \mu\text{m}$ and 45–90 μm	None	Pressureless sintering	$5 \times 5 \times 8$	16.0 ± 0.6	430 ± 22	This work
SC	45–90 μm	None	Pressureless sintering	$5 \times 5 \times 8$	20.8	294	
SD	45–90 μm	45–90 μm , 20 vol.%	Pressureless sintering	$5 \times 5 \times 8$	28.9 ± 1.4	208 ± 18	
SE	45–90 μm	180–250 μm , 20 vol.%	Pressureless sintering	$5 \times 5 \times 8$	33.2 ± 0.7	168 ± 27	
SF	45–90 μm	180–250 μm , 40 vol.%	Pressureless sintering	$5 \times 5 \times 8$	40.8 ± 0.8	149 ± 10	
SG	45–90 μm	355–500 μm , 20 vol.%	Pressureless sintering	$5 \times 5 \times 8$	34.0 ± 1.5	188 ± 12	

and tested along two loading directions, i.e. normal (σ_{\perp}) and parallel (σ_{\parallel}) to the aligned pore axis. The results of testing in compression and a schematic of loading direction vs. aligned pore axis are shown in Fig. 11e and f. The average value of σ_{\parallel} is 45% higher than that of σ_{\perp} , which is consistent with the results reported in the literature [49] for the samples with similar morphology, i.e. unidirectional pore alignment. As illustrated in Fig. 11f, the effective solid area parallel to the aligned pore axis is larger than that normal to the aligned pore axis, which most likely explains why the value of σ_{\parallel} is higher than that of σ_{\perp} . This indicates that the loading direction is an additional factor which should be taken into account for the evaluation of compressive strength of the porous Ti_2AlC samples with elliptical pores.

3.6. Room temperature thermal conductivity

Results of room temperature thermal conductivity measurements are summarized in Fig. 12. The thermal conduc-

tivity decreases significantly with increasing volume fraction porosity from 34 to 60 vol.%, while it hardly changes as the particle size of NaCl pore former changes from 45–90 μm to 180–250 μm to 355–500 μm . This suggests that porosity is an effective parameter for tailoring thermal conductivity, but pore size cannot significantly affect the magnitude of thermal conductivity. Fig. 12a shows that the experimental data agrees well with Bruggeman's model [50]:

$$\lambda_{\text{Eff}} = \lambda_{\text{MAX}}(1 - P)^{1.5} \quad (9)$$

where λ_{Eff} and λ_{MAX} represent the thermal conductivities of the porous Ti_2AlC and fully dense Ti_2AlC , respectively, and P is the volume fraction porosity.

The experimental data were also compared with theoretical bounds in Fig. 12b. Hashin and Shtrikman [51] derived effective conductivity bounds that were the narrowest bounds for macroscopically homogeneous, isotropic,

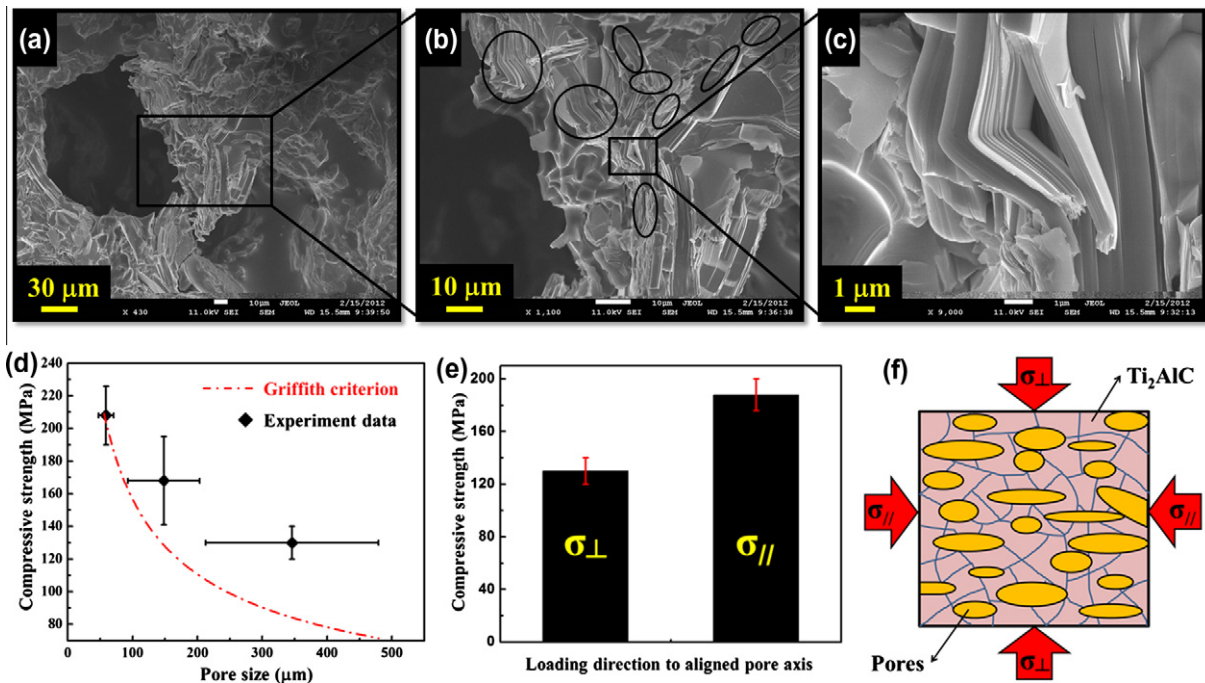


Fig. 11. Different magnification FE-SEM images of fracture surface of a compression tested sample processed using 40 vol.% NaCl pore former (180–250 μm), volume fraction of overall porosity = 41%: (a) $\times 430$, (b) $\times 1100$, and (c) $\times 9000$. Compressive strength as a function of (d) the particle size of NaCl pore former (the loading direction is normal to aligned pore axis), (e) loading direction, i.e. normal (σ_{\perp}) and parallel (σ_{\parallel}) to aligned pore axis (sample processed using 20 vol.% NaCl pore former (355–500 μm); and (f) schematic of the loading direction vs. the aligned pore axis. P : volume fraction of overall porosity.

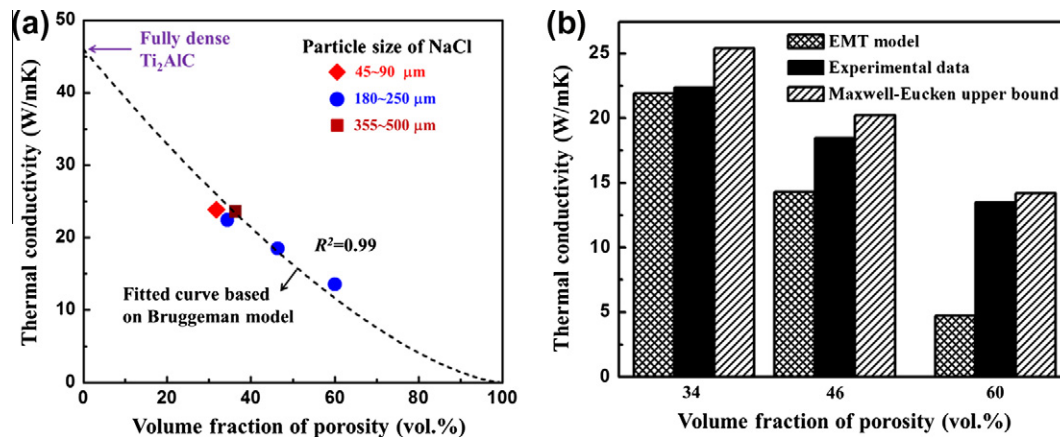


Fig. 12. (a) Room temperature thermal conductivity vs. volume fraction of overall porosity and pore size, i.e. particle size of NaCl pore former. (b) Comparison of the experimental results with the theoretical models, i.e. the EMT model and the Maxwell–Eucken upper bound.

two-phase materials. Their upper bound was mathematically equivalent to the well-known Maxwell–Eucken model:

$$\lambda_{\text{Eff}} = \lambda_{\text{MAX}} \frac{2\lambda_{\text{MAX}} + \lambda_{\text{Air}} - 2(\lambda_{\text{MAX}} - \lambda_{\text{Air}}) \cdot P}{2\lambda_{\text{MAX}} + \lambda_{\text{Air}} + (\lambda_{\text{MAX}} - \lambda_{\text{Air}}) \cdot P} \quad (10)$$

where λ_{Air} represents the thermal conductivity of air. The thermal conductivity of air and fully dense Ti_2AlC of $0.026 \text{ W m}^{-1} \text{ K}^{-1}$ [52–55] and $46 \text{ W m}^{-1} \text{ K}^{-1}$ [3], respectively, were used in this study. On the other hand, in a heterogeneous material structure in which the two components are distributed connectively, either component may form continuous heat conduction pathways, depending on the relative amounts of the components. Carson [56] developed Landauer's theory [57] and reported that the effective conductivity of this specific structure could be modeled well by the effective media theory (EMT) equation:

$$(1 - P) \frac{\lambda_{\text{MAX}} - \lambda_{\text{Eff}}}{\lambda_{\text{MAX}} + 2\lambda_{\text{Eff}}} + P \frac{\lambda_{\text{Air}} - \lambda_{\text{Eff}}}{\lambda_{\text{Air}} + 2\lambda_{\text{Eff}}} = 0 \quad (11)$$

The experimental data in Fig. 12b usually lie between the Maxwell–Eucken upper bound and the EMT model. The observed decline of thermal conductivity with increasing porosity could be explained by the microstructures developed within the porous Ti_2AlC : the large number of pores trap air, which is a better thermal insulator, i.e. lower thermal conductivity than the highly conductive Ti_2AlC , and these air-filled pores constitute obstacles against the heat transfer along the thickness direction; moreover, large amounts of interconnected pores made the ceramics grains not necessarily continuous or dispersed, blocking the heat conducting pathways and also contributing to the remarkably low level of thermal conductivity. In addition, the large number of pores and micro-sized interfaces provided significant photon scattering.

4. Summary and conclusions

In summary, the present work reported a simple and inexpensive method of processing porous Ti_2AlC with

controlled porosity and pore size using NaCl as a pore former. Porous Ti_2AlC with a wide range of porosity from 10 to 71 vol.% were processed using different volume fractions of NaCl pore former. The samples with pores that were uniformly distributed in the Ti_2AlC matrix were processed by varying both pore former particle size and pore former volume fraction. It was found that higher porosity could be achieved by using finer Ti_2AlC powders with the same volume fraction of NaCl pore former. The present processing method can also be used for processing porous Ti_2AlC with graded porosity, and thus graded functional properties, as demonstrated in this work. Elastic moduli decrease with increasing volume fraction of porosity, which agrees well with the exponential model, Hasselman model and composite spheres model. Compressive strength decreased with both increasing volume fraction porosity and increasing pore size. However, due to the kinking and kink band formation, that decrease is more moderate than in typical porous brittle media. Room temperature thermal conductivity decreased with increasing porosity, but hardly changed with increasing pore size. The experimental data of thermal conductivity were located between the predictions of the effective media theory model and the Maxwell–Eucken upper bound.

Acknowledgements

This work was supported by the US Air Force Office of Scientific Research, MURI Program (FA9550-09-1-0686) to Texas A&M University, with Dr. David Stargel as the program manager.

References

- [1] Barsoum MW. Prog Solid State Chem 2000;28:201.
- [2] Barsoum MW, Radovic M. In: Clarke DR, Fratzl P, editors. Annual review of materials research, vol. 41. Palo Alto, CA: Annual Reviews; 2011. p. 195.
- [3] Sun ZM. Int Mater Rev 2011;56:143.
- [4] Sun ZM, Hashimoto H, Zhang ZF, Yang SL, Tada S. Mater Trans 2006;47:170.

- [5] Radovic M, Barsoum MW, Ganguly A, Zhen T, Finkel P, Kalidindi SR, et al. *Acta Mater* 2006;54:2757.
- [6] Basu S, Obando N, Gowdy A, Karaman I, Radovic M. *J Electrochem Soc* 2011;159:C90.
- [7] Byeon JW, Liu J, Hopkins M, Fischer W, Garimella N, Park KB, et al. *Oxid Met* 2007;68:97.
- [8] Sundberg M, Malmqvist G, Magnusson A, El-Raghy T. *Ceram Int* 2004;30:1899.
- [9] Gupta S, Filimonov D, Zaitsev V, Palanisamy T, Barsoum MW. *Wear* 2008;264:270.
- [10] Barnes LA, Rago NLD, Leibowitz L. *J Nucl Mater* 2008;373:424.
- [11] Wang XH, Zhou YC. *J Mater Sci Technol* 2010;26:385.
- [12] Fraczkiewicz M, Zhou AG, Barsoum MW. *Acta Mater* 2006;54:5261.
- [13] Zhou AG, Barsoum MW, Basu S, Kalidindi SR, El-Raghy T. *Acta Mater* 2006;54:1631.
- [14] Sun ZM, Murugaiah A, Zhen T, Zhou A, Barsoum MW. *Acta Mater* 2005;53:4359.
- [15] Brodnikovskii NP, Burka MP, Verbilo DG, Demidik AN, Ivanova II, Koval AY, et al. *Powder Metall Met Ceram* 2003;42:424.
- [16] Firstov SA, Pechkovsky EP, Ivanova II, Brodnikovskiy NP, Gorban VF, Demidik AN. *High Temp Mater Process* 2006;25:47.
- [17] Firstov SA, Gorban VF, Ivanova II, Pechkovskii EP. *Powder Metall Met Ceram* 2010;49:414.
- [18] Amini S, Ni CY, Barsoum MW. *Compos Sci Technol* 2009;69:414.
- [19] Amini S, Barsoum MW. *Mater Sci Eng A – Struct Mater Prop Microstruct Process* 2010;527:3707.
- [20] Kontsos A, Loutas T, Kostopoulos V, Hazeli K, Anasori B, Barsoum MW. *Acta Mater* 2011;59:5716.
- [21] Ziqi S, Ying L, Meishuan L, Yanchun Z. *J Am Ceram Soc* 2010;93:2591.
- [22] Polonsky LLS, Markus H. *Mod Cast* 1961;39.
- [23] San Marchi C, Mortensen A. *Acta Mater* 2001;49:3959.
- [24] Despois JF, Marmottant A, Conde Y, Goodall R, Salvo L, San Marchi C, et al. In: Umakoshi Y, Fujimoto S, editors. *Advanced structural and functional materials design, proceedings*, vol. 512. Zurich-Uetikon: TransTech; 2006. p. 281.
- [25] Zhao YY, Sun DX. *Scripta Mater* 2001;44:105.
- [26] Bansiddhi A, Dunand DC. *Acta Biomater* 2008;4:1996.
- [27] Bansiddhi A, Dunand DC. *J Mater Res* 2009;24:2107.
- [28] Ye B, Dunand DC. *Mater Sci Eng A – Struct Mater Prop Microstruct Process* 2010;528:691.
- [29] Pekala RW, Hopper RW. *J Mater Sci* 1987;22:1840.
- [30] Fitzgerald TJ, Michaud VJ, Mortensen A. *J Mater Sci* 1995;30:1037.
- [31] Radovic M, Lara-Curzio E. *J Am Ceram Soc* 2004;87:2242.
- [32] Migliori A, Sarrao JL. *Resonant ultrasound spectroscopy: applications to physics, materials measurements, and nondestructive evaluation*. New York: John Wiley; 1997.
- [33] Radovic M, Lara-Curzio E, Riester L. *Mater Sci Eng A – Struct Mater Prop Microstruct Process* 2004;368:56.
- [34] Spencer CB, Cordoba JM, Obando N, Sakulich A, Radovic M, Oden M, et al. *J Am Ceram Soc* 2011;94:3327.
- [35] Turkdogan E. *Physical chemistry of high-temperature technology*. New York: Academic Press; 1980.
- [36] Barin I, Knacke O. *Thermochemical properties of inorganic substances*. Berlin: Springer-Verlag; 1973.
- [37] Sun ZM, Li S, Ahuja R, Schneider JM. *Solid State Commun* 2004;129:589.
- [38] Spriggs RM. *J Am Ceram Soc* 1961;44:628.
- [39] Knudsen FP. *J Am Ceram Soc* 1962;45:94.
- [40] Hasselman DPH. *J Am Ceram Soc* 1962;45:452.
- [41] Hashin Z. *Elasticity of ceramic systems*. Boulder, CO: Westview Press; 1977.
- [42] Ramakrishnan N, Arunachalam VS. *J Mater Sci* 1990;25:3930.
- [43] Ramakrishnan N, Arunachalam VS. *J Am Ceram Soc* 1993;76:2745.
- [44] Barsoum MW, Ali M, El-Raghy T. *Metall Mater Trans A – Phys Metall Mater Sci* 2000;31:1857.
- [45] Rice R. *Porosity of ceramics*. New York: Marcel Dekker; 1998.
- [46] Hu LF, Wang CA. *Ceram Int* 2010;36:1697.
- [47] Saito S. *Fine ceramics*. New York: Elsevier; 1988.
- [48] Griffith A. *Philos Trans Roy Soc Lond* 1920;A221.
- [49] Hu LF, Wang CA, Huang Y. *J Eur Ceram Soc* 2011;31:2915.
- [50] Bruggeman DAG. *Ann Phys Berlin* 1935;24:636.
- [51] Hashin Z, Shtrikman S. *J Appl Phys* 1962;33:3125.
- [52] Cao XQ, Vassen R, Stoeber D. *J Eur Ceram Soc* 2004;24:1.
- [53] Hu LF, Wang CA, Huang Y. *J Mater Sci* 2010;45:3242.
- [54] Hu LF, Wang CA, Hu ZJ, Lu S, Sun CC, Huang Y. *J Mater Sci* 2011;46:623.
- [55] Hu LF, Wang CA, Huang Y, Sun CC, Lu S, Hu ZJ. *J Eur Ceram Soc* 2010;30:3389.
- [56] Carson JK, Lovatt SJ, Tanner DJ, Cleland AC. *Int J Heat Mass Transfer* 2005;48:2150.
- [57] Landauer RJ. *Appl Phys* 1952;23:779.